Combined Differential Interferometry and Long-range PIV measurements of a temperature driven boundary layer flow

Kordel, S.; Nowak, T.; Skoda, R. et al.

(2016)

Combined Differential Interferometry and Long-range μPIV measurements of a temperature driven boundary layer flow

Combined Differential Interferometry and Long-range μPIV measurements of a temperature driven boundary layer flow

S Kordel[1], T Nowak[1], R Skoda[1] and J Hussong[1]

[1]Ruhr-Universität Bochum, Chair of Fluid Machinery, Universitätsstraße 150, 44801 Bochum, Germany

E-mail: stephan.kordel@ruhr-uni-bochum.de

Abstract. In the present study Differential Interferometry and Long-range μPIV are successfully combined for a benchmark experiment of an accelerating temperature driven boundary layer flow. Spatial resolutions of 405 µm for the interference and 101 µm for the μPIV measurements could be achieved. The results of the combined measurements are compared with results of numerical simulations. Temperature and velocity profiles are compared with theoretical values and a relation between Nusselt number and Grashof number could be worked out.

1. Introduction

Several optical measurement techniques are available nowadays that have been used for simultaneous measurements of velocity and temperature or concentration distributions. Praisner et al. [1] for example combined a liquid crystal sensing system and PIV to determine the convective heat transfer and the flow field of a turbulent water channel flow. In flow situations where transient scalar fields such as density or pressure distributions have to be determined, interference methods have been the first choice for many decades. The most common interference techniques for flow studies are Mach-Zehnder Interferometry (MZI) and Differential Interferometry (DI) [2]. Goldstein and Eckert [3] used a Mach-Zehnder Interferometer to the study the steady state and transient development of a free convection thermal boundary layer about a uniformly heated vertical plate. Early studies on simultaneous density and velocity field measurements were utilized by Skarman et al. [4]. They combined holographic interferometry with 3D-PTV measurements to capture temperature and flow fields. While interference techniques are often used to measure density fields in gas flows, applications to weakly compressible liquid flows are scarce [5]. Iben et al. [6] performed pressure field measurements in cavitating liquid flows by means of Mach-Zehnder Interferometry.

In the present work simultaneous velocity and temperature field measurements were successfully performed, combining for the first time Long-range PIV and Differential Interferometry with a standard double-pulsed Nd:YAG laser. In the present study we present results on the time dependent temperature and velocity fields in a temperature driven circulation flow in a cuvette that was created by a heated side wall.

(a) (b)

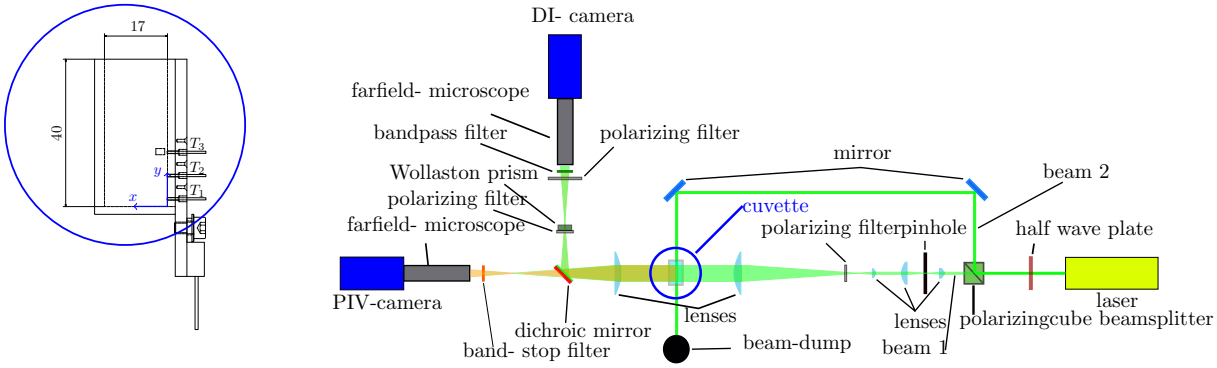

Figure 1: (a) Side view of cuvette; thermocouples are indicated with T_1 to T_3; (b) Optical set-up of the combined measurement technique

2. Set-up

2.1. Optical System

The experimental set-up of the combined measurement technique of Long-range µPIV and Differential Interferometry (DI) as shown in Fig.1b was established and tested. Details can be found in Kordel et al [7]. A double pulsed dual cavity Nd:YAG laser (Nano S 65-15 PIV, Nitron Lasers, $\lambda = 532\,\text{nm}$) is used at a frequency of 5 Hz. Using a combination of a half wave plate and a polarizing beam splitter cube the pulsed beam is split into two separate parts of approximately 5 % (beam 1) and 95 % (beam 2) laser intensity. After passing a spatial filter system beam 1 is widened to a bundle of parallel light which passes the test section in positive z-direction. The second beam (beam 2) is deflected unchanged in such a way that it enters the test section in negative x-direction. Suspended Rhodamine B coated fluid tracers (Microparticles GmbH) of $25.07 \pm 0.2\,\mu\text{m}$ nominal diameter in the middle plain of the test section (z=0) are excited in means of a volume illumination by the laser beam. Both, the laser light and the fluorescence signal are passing along z-axis, are then focused by a lens before separated again by a dichroic mirror. While the particle light transmits the dichroic mirror and is then recorded directly by a 12 bit dual frame CCD camera (Imager Pro SX, LaVision) the laser light is reflected. The reflected laser light passes a Wollaston prism and a polarizer which creates interference fringes in the image plane. Two far-field microscopes (Infinity K2, DistaMax) with 2.18 x magnification yield a field of view (FOV) of 3.246 mm x 3.874 mm for the full camera sensor of 2456 x 2058 pixel.

2.2. Measurement Section

An optically accessible cuvette (Hellma GmbH Co. KG) is used for all measurements (see Fig. 1a). The cuvette has a thickness of $b = 10\,\text{mm}$ and one side wall was replaced by a brass plate. It is closed with a plastic plug to avoid a free surface. Heat is supplied to the plate by a $10\,\Omega$ resistor and a 4 W power supply. Along the y-axis the near wall water temperature is measured by three thermocouples (T_1 - T_3) which reach approximately 400 µm into the fluid and have a spacing of 2 mm, 8 mm and 14 mm to the bottom wall of the cuvette.

3. Measurement procedure

For all measurements a total time series of 60 s at a frequency of 5 Hz was recorded. The heating process was started with 2 s delay to measure the initial fluid temperature (ambient

temperature) and eventual background flows in the cuvette. At each time step both, DI and µPIV camera, record a double image pair. This leads to a total amount of 600 double images for one measurement sequence. The interframing time was set to $dt = 5\,\mathrm{ms}$. Hence, the particle image displacement is $\sim 10\,\mathrm{pixel}$ in the final stage of the measurement sequence. Due to refraction effects in the DI image the particle image density for the used 25.07 µm Rhodamine B particles was limited to $3.9 \times 10^{-4}\,\mathrm{particle\,pixel}^{-1}$ within the FOV. The orientation of the fringe pattern can be adopted by the rotation Wollaston prism. In this evaluation all measurements are done with an fringe orientation angle of $\alpha = \pm 45°$.

4. Evaluation

4.1. Differential Interferometry

An in-house matlab code is used for the evaluation of the recorded interferograms. It evaluates the density gradient based on the relative fringe displacement $\Delta S/S$ as follows [8]:

$$\frac{\partial \overline{\rho}(x,y)}{\partial \zeta} = \frac{\lambda}{Kbd}\frac{\Delta S(x,y)}{S} \tag{1}$$

Here, ζ denotes the direction normal to the fringe orientation. K is the Gladstone-Dale constant which was evaluated for a temperature range of $20\,°\mathrm{C} \leq T \leq 40\,°\mathrm{C}$. Wavelength λ, measurement volume thickness d and the distance between neighboring light rays b [9] are characteristic quantities of the set-up and constant throughout all measurements.
To determine $\Delta S/S$ a fourth order polynomial was fitted to each fringe of the pattern and was then compared to a linear equation extracted from a initial not displaced reference fringe. The local gradient evaluation by the fringe pattern limits the spatial resolution to the fringe spacing S. In order to receive a continuous fringe displacement field a 2D surface polynomial was fitted to the displacement values. From this the density gradient field in ζ-direction was derived. Hence, this is not necessary the gradients main direction, measurements are repeated with 90° rotated Wollaston prism. Again the density gradient field, now in η direction is determined. A final coordinate transformation gives the gradient in x-and y-direction.
With a reference temperature from the thermocouples the temperature field can be derived by integration [10].
To compensate for refraction effects, which may lead to an overestimation of the density gradient, an a priory calibration procedure was implemented in the set-up. With the help of a calibration plate and a blue LED the refraction induced image distortion is measured by means of an Background Oriented Schlieren (BOS) evaluation. A mapping function for each time step is applied for fringe image.

4.2. Long-range µPIV

The evaluation of the recorded particle images is done with commercial software DaVis 8.2.2 (LaVision GmbH). Before the evaluation of the particle image shift several preprocessing steps are performed to improve the signal-to-noise ratio reaching a mean background signal of about 0.16 counts. The PIV evaluation uses a 2D multi-pass cross-correlation algorithm. To achieve reliable cross-correlation results of more than 95 % probability the particle density has to be > 5 per interrogation window [11]. Therefore, a final window size of 128 x 128 pixel with 5 % overlapping was chosen, leading to a vector spacing of 101 µm.

5. Results

5.1. Temperature and Velocity fields

Figs. 2a and 2b show the temperature and a velocity field within a Region of Interest (ROI) of $0.82\,\mathrm{mm} \leq \Delta x \leq 3\,\mathrm{mm}$ spacing to the heated side wall and $12.8\,\mathrm{mm} \leq \Delta y \leq 15.5\,\mathrm{mm}$ spacing to the bottom wall of the combined measurement technique at $t = 30\,\mathrm{s}$. Since a fully transient

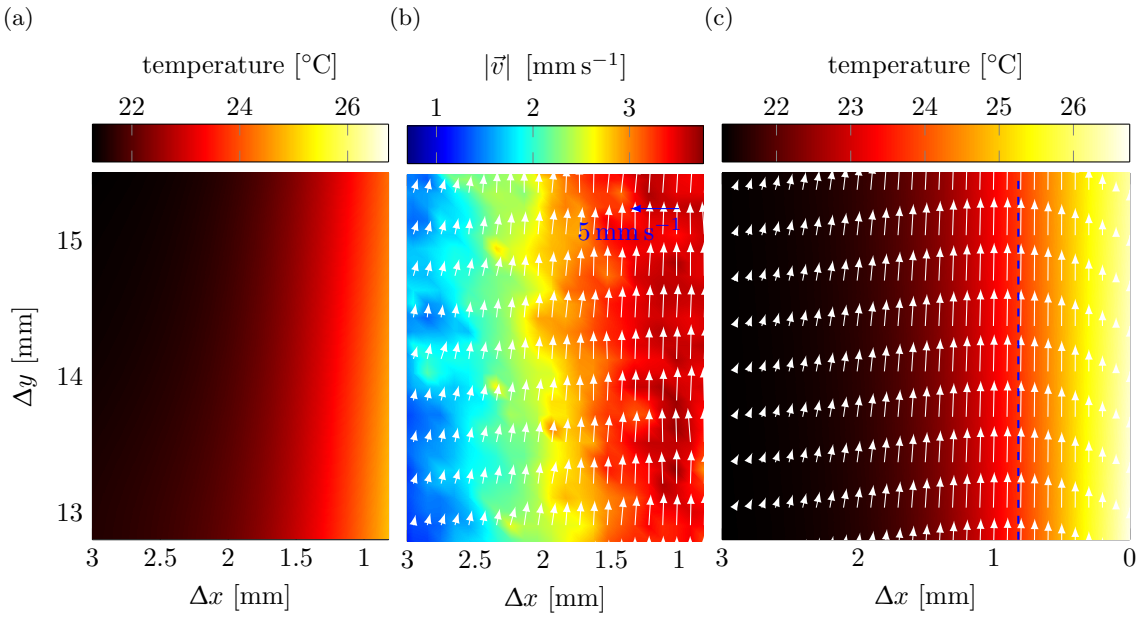

Figure 2: (a) Measured temperature field; (b) Measured velocity field; (c) Temperature field (contour plot) and velocity field (vectors) derived from simulations; Experimental and numerical results at $t = 30\,\mathrm{s}$

flow is investigated, the velocity field (see Fig. 2b) is computed by cross-correlation of one double image pair. As mentioned in section 4.1 the temperature field (Fig. 2a) is a result of two separate measurements. Out of three independent repetitive measurements the local maximum standard deviation of measured density gradient fields in ζ direction was determined to be less than $\delta_{max} = 4\,\%$. Hence, the computation of the main density gradient out of two measurements is a fair procedure. Nevertheless, our aim in future studies is to record the density gradients in ζ and η direction simultaneously. Therefore a second Wollaston prism is needed, which will be placed in a separated beam path before recombined again. The result is a grid pattern as discussed in section 6.

Fig. 2c shows results of numerical simulations at the same time step. The three dimensional flow problem has been simulated using ANSYS CFX. For simulations both, the brass plate and the fluid have been modeled with cuboid elements on a Cartesian grid. The first 3 mm spacing to the heated side wall were resolved with 300 elements in x-direction with 4.6 million cells in the domain. The heat source is represented by a point source supplying 4 W. For the brass plate a specific heat capacity of $376\,\mathrm{J\,kg^{-1}\,K^{-1}}$ and a heat transfer coefficient of $454\,\mathrm{W\,m^{-2}\,K^{-1}}$ for the heat transfer between brass and fluid have been estimated. Glass walls are modeled with no slip wall boundary conditions and a heat transfer coefficient of $5.1\,\mathrm{W\,m^{-2}\,K^{-1}}$.

Both, experimental and numerical results are in good agreement. Local temperature deviations of up to 1.2 °C in the near wall region can be detected. Our assumption is that these differences originate from deviations in the actual and numerically assumed heat transfer coefficient and power input, which lead to different wall temperatures in the simulation and the experiment. As the actual alloy composition for the used brass wall is unknown the heat transfer coefficient was assumed from standard material tables [12].

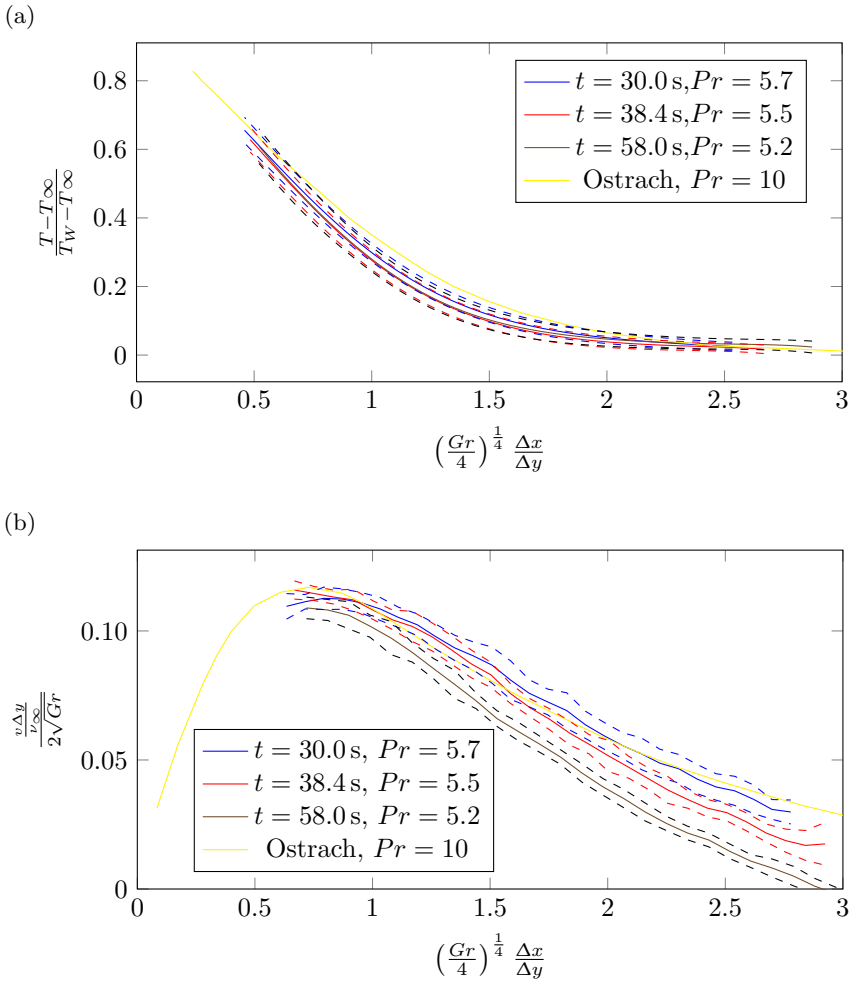

Figure 3: (a) Dimensionless temperature profiles and (b) Dimensionless velocity magnitude profiles in the dimensionless normal wall direction Δx for height of $\Delta y = 14\,\mathrm{mm}$ from the bottom wall at different time steps; yellow indicated theoretical computations of Ostrach [13]

5.2. Temperature and Velocity profiles of the accelerating flow

Fig. 3 shows the temperature and velocity profiles of the wall normal direction Δx averaged over $12.8\,\mathrm{mm} \leq \Delta y \leq 15.5\,\mathrm{mm}$ and the corresponding standard deviation as a function of time and therefore of the Prandtl number. The profiles are shown for $0.82\,\mathrm{mm} \leq \Delta x \leq 3$ which corresponds to the depicted ROI. Because of the steady growth of the temperature profile a time independent and dimensionless scale was chosen. For comparison theoretical profiles for a laminar convection flow of a vertical plate with homogeneous temperature distribution according to Ostrach [13] are plotted in yellow for a Prandtl number of 10. The Prandtl number decreases with higher temperature and in this case with higher velocities. The profiles are in good qualitative agreement with theoretical predictions. Differences emanate from different inflow conditions of the present experimental compared to those depicted by Ostrach.

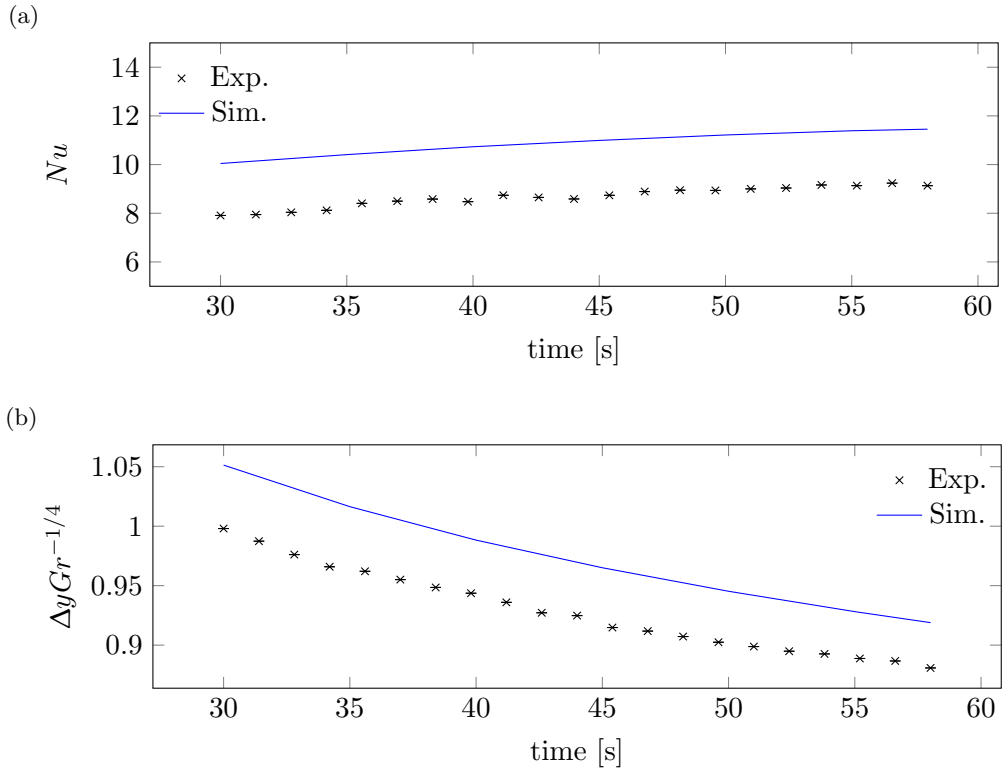

Figure 4: (a) Nusselt numbers averaged over for 12.8 mm $\leq \Delta y \leq$ 15.5 mm according to (2) at different time steps; (b) averaged scaled Grashof number $\Delta y Gr^{-1/4}$ for 12.5 mm $\leq \Delta y \leq$ 15.5 mm

Additionally Nusselt and Grashof numbers were determined according to:

$$Nu = \frac{\Delta y \cdot \frac{\partial T}{\partial x}|_w}{(T_w - T_\infty)} \tag{2}$$

$$Gr = \frac{g \Delta y^3 \beta_{inf} \left(T_w - T_\infty\right)}{\nu_{inf}^2} \tag{3}$$

$$\bar{\delta_h} \propto \Delta y Gr^{-1/4} \tag{4}$$

Here, $\Delta y = 14$ mm denotes the distance from the bottom wall. $\partial T/\partial x$ is the temperature gradient in normal wall direction and T_w the wall temperature. Both values were extracted from a first order polynomial fit to the temperature profiles. $T_\infty = 21.2\,^\circ$C denotes the starting temperature of the fluid measured by the thermocouples, g denotes the acceleration of gravity, β is the isobaric cubic expansion coefficient and ν is the kinematic viscosity for water at $T = 21.2\,^\circ$C. $\bar{\delta_h}$ denotes the hydrodynamic boundary layer thickness.

Since there is a proportionality between Grashof number and hydrodynamic boundary layer thickness according to (4), Nu and $\Delta y Gr^{-1/4}$ are shown in Fig.4a and 4b.

Fig. 4 shows the Nusselt numbers and the hydraulic boundary layer thickness as a function of time for both, numerical and experimental results. While in both cases the slopes are similar, there is an offset between the absolute values. It may be noted that both, Nusselt number and Grashof number are mainly a function of wall temperature and as mentioned in section 5.1, the near wall temperature in the simulation differs from that in the actual experiment.
Early studies of Goldstein and Eckert [3] showed that the unsteady free convection boundary

layer grows with time before shrinking again to approach a steady state value. Obviously the time series shown here, covers the phase of hydrodynamical boundary layer shrinking. According to a relation obtained by Sparrow and Gregg [14] for this phase of flow problem following relation can be expressed:

$$Nu = k \cdot \left(\frac{GrPr}{4}\right)^{1/4} \tag{5}$$

It could be found that the factor $k \approx 0.5$ here for $Pr = 5.7$.

6. Conclusion and Outlook

Combined Differential Interferometry and Long-range µPIV measurements could be successfully applied to a temperature driven boundary layer flow. Spatial resolutions of 405 µm for Differential Interferometry and 101 µm for Long-range µPIV could be achieved. The comparison between measurement and simulations results showed local temperature deviations of less than 1.2 °C, which lead to deviations in the temporal evolution of the Nusselt number and the thickness of the hydrodynamic boundary layer at the same time. While the Nusselt numbers increased for all observed time steps, the hydrodynamics boundary layer reduces simultaneously. Theoretical results of a steady laminar convective flow with a vertical heated plate are in good qualitative agreement to the observed flow problem.
In future studies the measurement technique will be improved by implementing a second Wollaston Prism into the set-up. For this the separated laser light after the dichroic mirror (see Fig 1b) has to be split into two parallel beams each passing one Wollaston prism. Before entering the camera the signals have to be recombined again. The result on the camera chip is a grid pattern. Furthermore, to investigate all characteristics of the boundary layer development, long time scale measurement are planned.

References

[1] Praisner T J, Sabatino D R and Smith C R 2001 *Experiments in Fluids* **30** 1–10
[2] Egbers C, Brasch W, Sitte B, Immohr J and Schmidt J R 1999 *Measurement Science and Technology* **10** 866–877
[3] Goldstein R and Eckert E 1960 *International Journal of Heat and Mass Transfer* **1**
[4] Skarman B, Becker J and Wozniak K 1996 *Flow Measurement and Instrumentation* **7** 1–6
[5] Woisetschläger J, Pretzler G, Jericha H, Mayrhofer N and Pirker H P 1998 *Experiments in Fluids* **24** 102–109
[6] Iben U, Morozov A, Winklhofer E and Wolf F 2011 *Experiments in Fluids* **50** 597–611
[7] Kordel S, Nowak T, Skoda R and Hussong J (accepted) 2016 *Experiments in Fluids*
[8] Merzkirch W 1987 *Flow visualization* 2nd ed (Orlando: Acad. Press)
[9] Small R D, Sernas V A and Page R H 1972 *Applied Optics* **11** 858
[10] Agrawal A, Raskar R and Chellappa R 2006 *Computer Vision ECCV 2006* vol 3951 (Berlin, Heidelberg: Springer Berlin Heidelberg) pp 578–591
[11] Raffel M (ed) 2007 *Particle image velocimetry: a practical guide* 2nd ed (Heidelberg ; New York: Springer)
[12] Verein Deutscher Ingenieure and Gesellschaft Verfahrenstechnik und Chemieingenieurwesen (eds) 2013 *VDI-Wärmeatlas* 11th ed (Berlin: Springer Vieweg)
[13] Ostrach S 1953 *Trans. Am. Soc. Mec. Engrs* **75** 1287–1290
[14] Sparrow E and Gregg J 1956 *Trans. ASME* **78** 435–440